

High-performance bulk thermoelectrics with all-scale hierarchical architectures

David N Seidman


Nature

Cite this paper

Downloaded from [Academia.edu](#) 

[Get the citation in MLA, APA, or Chicago styles](#)

Related papers

[Download a PDF Pack](#) of the best related papers 



[Thermoelectric materials: Energy conversion between heat and electricity](#)

Shetti Swamy

[High-Performance Tellurium-Free Thermoelectrics: All-Scale Hierarchical Structuring of p-Type PbSe...](#)

Duck-Young Chung

[High Performance Thermoelectrics from Earth-Abundant Materials: Enhanced Figure of Merit in PbS ...](#)

Duck-Young Chung

High-performance bulk thermoelectrics with all-scale hierarchical architectures

Kanishka Biswas^{1†}, Jiaqing He^{1,2†}, Ivan D. Blum², Chun-I Wu³, Timothy P. Hogan³, David N. Seidman², Vinayak P. Dravid² & Mercouri G. Kanatzidis^{1,4}

With about two-thirds of all used energy being lost as waste heat, there is a compelling need for high-performance thermoelectric materials that can directly and reversibly convert heat to electrical energy. However, the practical realization of thermoelectric materials is limited by their hitherto low figure of merit, ZT , which governs the Carnot efficiency according to the second law of thermodynamics. The recent successful strategy of nanostructuring to reduce thermal conductivity has achieved record-high ZT values in the range 1.5–1.8 at 750–900 kelvin^{1–3}, but still falls short of the generally desired threshold value of 2. Nanostructures in bulk thermoelectrics allow effective phonon scattering of a significant portion of the phonon spectrum, but phonons with long mean free paths remain largely unaffected. Here we show that heat-carrying phonons with long mean free paths can be scattered by controlling and fine-tuning the mesoscale architecture of nanostructured thermoelectric materials. Thus, by considering sources of scattering on all relevant length scales in a hierarchical fashion—from atomic-scale lattice disorder and nanoscale endotaxial precipitates to mesoscale grain boundaries—we achieve the maximum reduction in lattice thermal conductivity and a large enhancement in the thermoelectric performance of PbTe. By taking such a panoscopic approach to the scattering of heat-carrying phonons across integrated length scales, we go beyond nanostructuring and demonstrate a ZT value of ~ 2.2 at 915 kelvin in p-type PbTe endotaxially nanostructured with SrTe at a concentration of 4 mole per cent and mesostructured with powder processing and spark plasma sintering. This increase in ZT beyond the threshold of 2 highlights the role of, and need for, multiscale hierarchical architecture in controlling phonon scattering in bulk thermoelectrics, and offers a realistic prospect of the recovery of a significant portion of waste heat.

The performance of a thermoelectric material is quantified by $ZT = \sigma S^2 / (\kappa_{el} + \kappa_{lat})$, where σ is the electrical conductivity, S is the Seebeck coefficient, T is the temperature, κ_{el} is the electronic thermal conductivity and κ_{lat} is the lattice thermal conductivity^{4,5}. Among the high- ZT materials, PbTe (refs 1–3) is the most efficient for power-generation applications at high temperature, whereas Bi₂Te₃-based materials^{6,7} are renowned for refrigeration near room temperature. Several innovative strategies have recently been introduced to increase the ZT value of PbTe (refs 1–3). Nanostructuring, in particular, has been proven to be an effective approach to enhance ZT by reducing κ_{lat} through the placement of suitable nanoscale precipitates in the matrix, for example in AgPb_mSbTe_{m+2} (ref. 8; LAST), NaPb_xSbTe_{2+x} (ref. 9; SALT) and PbTe–PbS (ref. 10). Alternatively, p-type PbTe_{1–x}Se_x (ref. 11) and Tl–PbTe (ref. 12) also have excellent thermoelectric properties, arising from multiple valence bands and the introduction of a density-of-states distortion in the valence band, respectively. Skutterudite structures have also been shown to have high ZT values¹³. Yet, despite remarkable progress, all state-of-the-art materials have ZT

values in the range of 1.5–1.8 at 750–900 K, well below the target of 2 sought in the field.

Optimized atomic-scale doping/substitution (Fig. 1a) in the PbTe structure can lead to a ZT value of ~ 1.1 at 775 K (Fig. 1b) in the case of a bulk ingot sample of PbTe doped with 2 mol% Na. The maximum

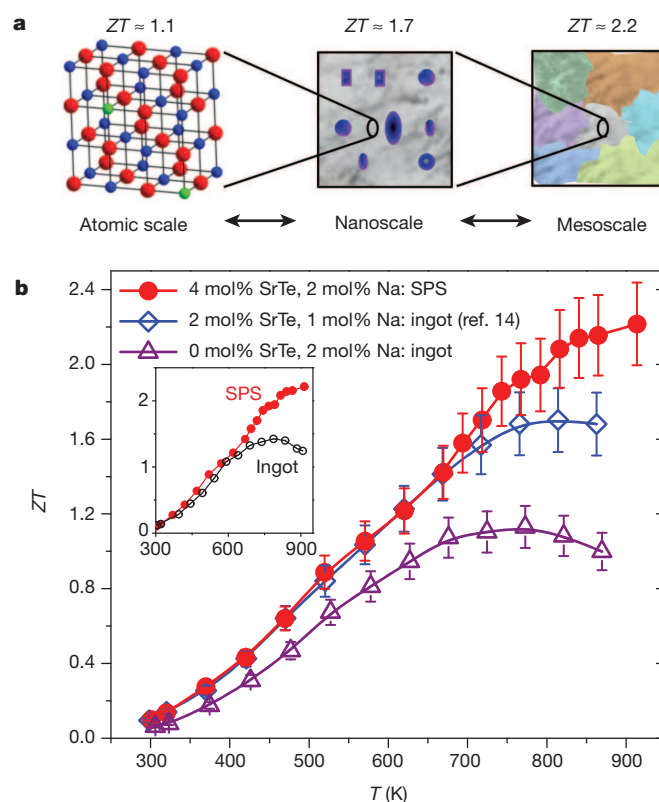


Figure 1 | All-length-scale hierarchy in thermoelectric materials.

a, Maximum achievable ZT values for the respective length scales: the atomic scale (alloy scattering: red, Te; blue, Pb; green, dopant), the nanoscale (PbTe matrix, grey; SrTe nanocrystals, blue) to the mesoscale (grain-boundary scattering). By combining the effects of atomic-scale alloy doping, endotaxial nanostructuring and mesoscale grain-boundary control, maximum phonon scattering can be achieved at high temperatures and the figure of merit can be increased beyond the value possible with nanostructuring alone. **b**, ZT as a function of temperature for an ingot of PbTe doped with 2 mol% Na (atomic scale), PbTe–SrTe(2 mol%) doped with 1 mol% Na (ref. 14; atomic plus nanoscale) and spark-plasma-sintered PbTe–SrTe(4 mol%) doped with 2% Na (atomic plus nano plus mesoscale). The measurement uncertainty of all experimental ZT versus T data was 10% (error bars). Inset, comparison of ZT in SPS and ingot samples with the same composition (PbTe–SrTe(4 mol%) doped with 2 mol% Na).

¹Department of Chemistry, Northwestern University, Evanston, Illinois 60208, USA. ²Materials Science and Engineering, Northwestern University, Evanston, Illinois 60208, USA. ³Department of Electrical and Computer Engineering, Michigan State University, East Lansing, Michigan 48824, USA. ⁴Materials Science Division, Argonne National Laboratory, Argonne, Illinois 60439, USA. [†]Present addresses: New Chemistry Unit, Jawaharlal Nehru Centre for Advanced Scientific Research (JNCASR), Jakkur, Bangalore 560064, India (K.B.); Frontier Institute of Science and Technology (FIST), Xi'an Jiaotong University, Xi'an 710054, China (J.H.).

ZT value increases to ~ 1.7 at 800 K (Fig. 1b) on the introduction of 2–10-nm endotaxial SrTe nanocrystals (Fig. 1a) into the Na-doped PbTe matrix¹⁴. This performance increase stems from the fact that the nanostructures impede much of the heat flow in this system while leaving the hole mobility largely unaffected¹⁴. Nanostructuring itself, however, scatters phonons with short and medium mean free paths (~ 3 –100 nm), thus rendering only phonons with longer mean free paths unaffected. An additional and significant reduction in κ_{lat} may be achieved by further scattering of the phonons with longer mean free paths (~ 0.1 –1 μm , that is, mesoscale; Fig. 1a), on which scale additional mechanisms of grain-boundary phonon scattering and impedance can be exploited. Grain-boundary phonon scattering has been shown to be important in improving the thermoelectric performance of Bi_2Te_3 -based alloys, PbTe and nanostructured silicon^{6,15,16}.

Here we go beyond nanostructuring and show that by harnessing integrated phonon scattering across multiple length scales—atomic-scale alloy scattering, scattering from nanoscale endotaxial precipitation

and scattering from mesoscale grain boundaries—we can achieve a record-high ZT value of ~ 2.2 at 915 K (Fig. 1b) in powder-processed and spark-plasma-sintered (SPS) samples of PbTe–SrTe(4 mol%) doped with 2 mol% Na. Compared with melt-processed ingot specimens of the same composition (Fig. 1b, inset), SPS specimens show a ~ 30 –50% increase in ZT , underscoring the role of integrated all-length-scale scattering of heat-carrying phonons as reflected in a reduced κ_{lat} value. This represents a panoscopic approach (a hierarchical architecture across all relevant length scales) to tackling the challenge of increasing ZT , and is an excellent example of a bulk system in which all relevant length scales are harnessed for achieving effective and efficient phonon scattering and, consequently, a record-high value of ZT . This approach is applicable to all bulk thermoelectric materials.

Samples of composition PbTe–SrTe(0–4 mol%) doped p -type with 2 mol% Na were synthesized in ingot form by melting and quenching, followed by powder processing and spark plasma sintering into dense pellets ($>98\%$ of the theoretical density). The temperature-dependent

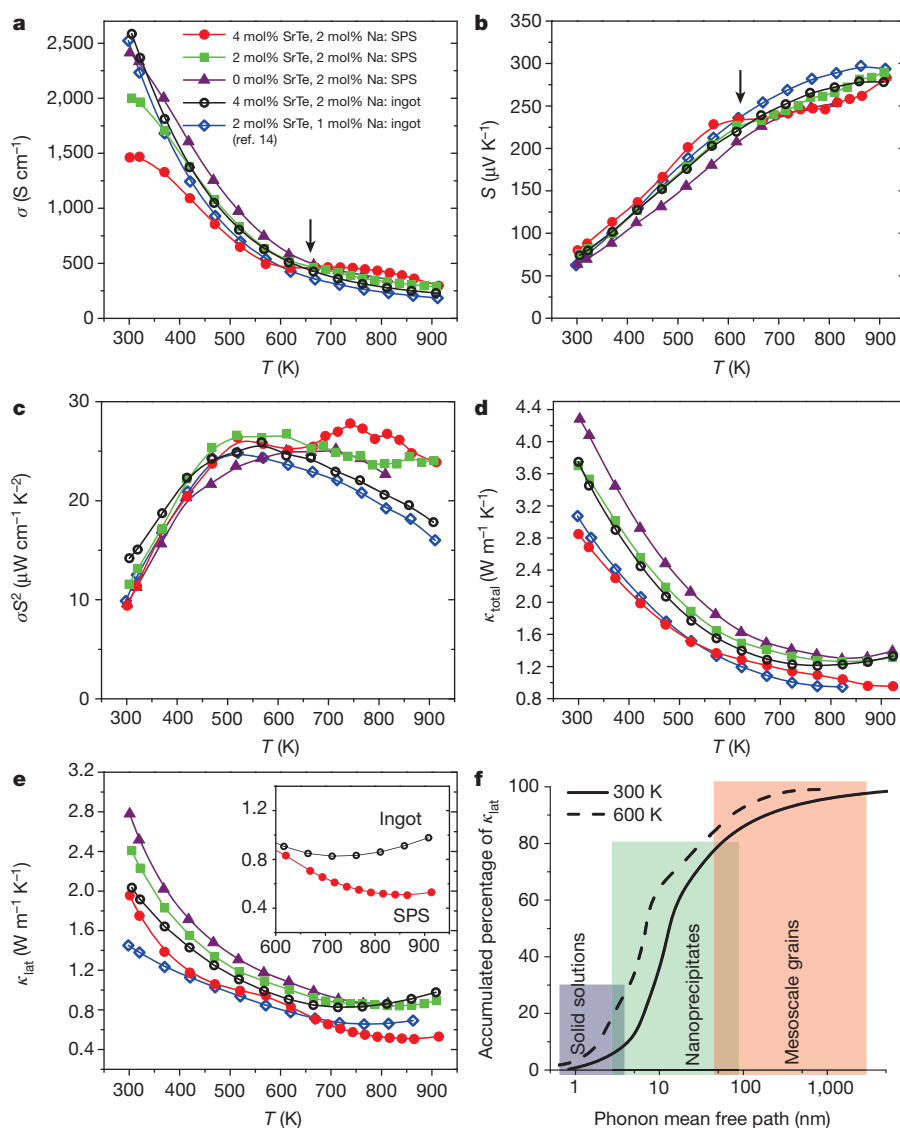


Figure 2 | Thermoelectric properties of SPS and ingot samples of PbTe–SrTe doped with 2 mol% Na. **a**, Temperature-dependent electrical conductivity (σ). The same symbol notation for the samples is used in all panels. The temperature-dependent transport data for the bulk ingot of PbTe–SrTe(2 mol%) doped with 1 mol% Na (ref. 14) is shown for comparison. **b–e**, Temperature-dependent Seebeck coefficient (S ; **b**), power factor (σS^2 ; **c**), total thermal conductivity (κ_{total} ; **d**) and lattice thermal conductivity (κ_{lat} ; **e**). Inset in **e**, comparison of κ_{lat} in SPS and ingot samples with the same

composition (PbTe–SrTe(4 mol%) doped with 2 mol% Na). **f**, Contributions of phonons with different mean free paths to the cumulative κ_{lat} value for PbTe, adapted from the literature²³. Phonons with short, medium and long mean free paths can be scattered by atomic-scale defects, nanoscale precipitates and mesoscale grain boundaries, respectively. Black arrows in **a** and **b** indicate the temperature of onset of Na diffusion in Na-doped PbTe, which results in the observed plateaux, starting at ~ 650 K, in σ and S as functions of T .

electrical and thermal transport properties of several such samples in the 300–950 K range are given in Fig. 2. The transport measurements of SPS samples were compared to the corresponding bulk ingot samples, and also with a previously reported ingot of PbTe–SrTe(2 mol%) doped with 1 mol% Na (ref. 14). Typically, the 2 mol% Na doped SPS sample containing 4 mol% SrTe has a electrical conductivity of $\sigma \approx 1,465 \text{ S cm}^{-1}$ at room temperature, which decreases to $\sim 457 \text{ S cm}^{-1}$ at 620 K, remains almost at that value in the 620–850 K range and reaches a value of $\sim 300 \text{ S cm}^{-1}$ at $\sim 915 \text{ K}$ (Fig. 2a). Ingot samples with the same nominal composition (PbTe–SrTe(4 mol%) doped with 2 mol% Na) show the room-temperature value of $\sigma \approx 2,585 \text{ S cm}^{-1}$, which decreases to $\sim 230 \text{ S cm}^{-1}$ at 910 K (Fig. 2a). The σ values of the SPS samples are higher at high temperatures, and effectively reach a plateau from 600 to 850 K. This causes the power factor, σS^2 , to remain high at higher temperatures. We attribute this rise in σ at high temperature to the enhanced dissolution in the PbTe matrix of the Na dopant, which at lower temperatures remains confined and segregated at grain boundaries, following powder and spark plasma sintering. This enhanced dissolution lowers the Fermi level further and generates new charge-carrier holes particularly in the ‘heavy-hole’ valence band of PbTe (refs 17–19). We confirmed the proposed segregation of Na at grain boundaries, precipitate–matrix interfaces and dislocations with three-dimensional atom probe tomography (APT; see below).

The Seebeck coefficient, S , is in agreement with the Hall measurements (Supplementary Information) for p-type PbTe (Fig. 2b). Typically, at room temperature the 4 mol% SrTe SPS sample doped with 2% Na has $S \approx 81 \mu\text{V K}^{-1}$, which rapidly increases with temperature, remains almost constant in the 600–850 K range and then reaches a value $\sim 284 \mu\text{V K}^{-1}$ at $\sim 915 \text{ K}$ (Fig. 2b). The high values of S at high temperature arise from the well-known contribution of the two valence bands in PbTe (refs 14, 17–19).

Figure 2c shows the power factors of different SPS and ingot PbTe–SrTe samples doped with 2% Na, as functions of temperature. Compared with ingots, the SPS samples have higher σS^2 values at higher temperatures, 600–915 K, because of the higher σ values in this range. Typically, the room-temperature σS^2 value we measured was $\sim 9.5 \mu\text{W cm}^{-1} \text{ K}^{-2}$ for the 4 mol% SrTe SPS sample doped with 2% Na. This value rose to a maximum ($\sim 28 \mu\text{W cm}^{-1} \text{ K}^{-2}$) at about 745 K and fell to $\sim 24 \mu\text{W cm}^{-1} \text{ K}^{-2}$ at $\sim 915 \text{ K}$.

The total thermal conductivity, κ_{total} , of the various samples is shown in Fig. 2d. A typical room-temperature value of $\kappa_{\text{total}} \approx 2.85 \text{ W m}^{-1} \text{ K}^{-1}$ was observed for PbTe–SrTe(4 mol%) SPS samples doped with 2% Na, which decreased to $\sim 0.96 \text{ W m}^{-1} \text{ K}^{-1}$ at $\sim 923 \text{ K}$. The electrical thermal conductivity ($\kappa_{\text{el}} = L\sigma T$, where L is the Lorenz number) was estimated on the basis of an L value obtained from the accepted approach of fitting the Seebeck data to the reduced chemical potential^{10,20,21} (Supplementary Fig. 6). The lattice thermal conductivity, κ_{lat} , was estimated by subtracting κ_{el} from κ_{total} (Fig. 2e). We observe that the κ_{lat} values of the SPS samples are lower than those of the ingots with the corresponding compositions and, more importantly, that the difference increases as the temperature is increased (Fig. 2e, inset), which leads to significantly depressed values at $\sim 900 \text{ K}$ compared with the ingots. The upturn in the plot of κ_{lat} as a function of T at high temperature for the ingot sample is due to the bipolar contribution to the thermal conductivity by thermally generated electrons and holes²². In contrast, in the SPS samples the bipolar contribution is negligible and there is no upturn because of the existence of an interfacial potential at grain boundaries that scatters more electrons than holes⁶. In addition, the overall decrease in the κ_{lat} value of the SPS sample compared with the corresponding ingot can be attributed to the additional scattering from and impedance due to mesoscale grain boundaries in the SPS sample, which is important in reducing bipolar conduction and scattering phonons with longer mean free paths, which generally are largely ignore nanostructuring.

The contributions to κ_{lat} of phonons with different mean free paths have recently been calculated for PbTe (refs 23, 24; Fig. 2f), PbTe_{1–x}Se_x (ref. 24) and Si (ref. 25). Around $\sim 80\%$ of the κ_{lat} value of PbTe is contributed by phonon modes with mean free paths of less than 100 nm, which can be attributed to scattering by a combination of atomic-scale solid-solution alloying, nanoscale precipitates embedded in PbTe and associated spatially distributed strain²³ (Fig. 2f). The remaining $\sim 20\%$ of κ_{lat} in PbTe, however, is contributed by phonon modes with mean free paths of 0.1–1 μm . The mesoscale grain structure, achieved by spark plasma sintering, is comparable in size to the mean free path and thus can scatter a notable fraction of these additional heat-carrying phonons. This results in further reduction of κ_{lat} , compared with nanostructuring alone.

The SPS samples contain nanoscale precipitates and mesoscale grains and associated grain boundaries, which are clearly evident in transmission electron microscopy (TEM) and APT studies. Detailed microstructure investigations using TEM were carried out on the SPS PbTe–SrTe(4 mol%) sample doped with 2 mol% Na. Typical low- and middle-magnification TEM images are shown in Fig. 3a and Fig. 3b, respectively. The presence of mesoscale grains 0.1–1.7 μm in size and nanoscale precipitates with dark contrasts in the range of 1–17 nm is evident in these images. The nanoscale precipitates have two typical shapes, platelet-like and spherical/ellipsoidal, with three crystallographic variants consistent with bicrystal symmetry. The small precipitates (~ 1 –6 nm) have a platelet-like morphology and are coherently strained, whereas the larger precipitates (~ 10 –17 nm) have spherical or ellipsoidal shapes along with interfacial misfit dislocations. The latter arise from excess coherency strain that derives from the small lattice parameter mismatch (6.460 Å versus 6.660 Å for PbTe and SrTe,

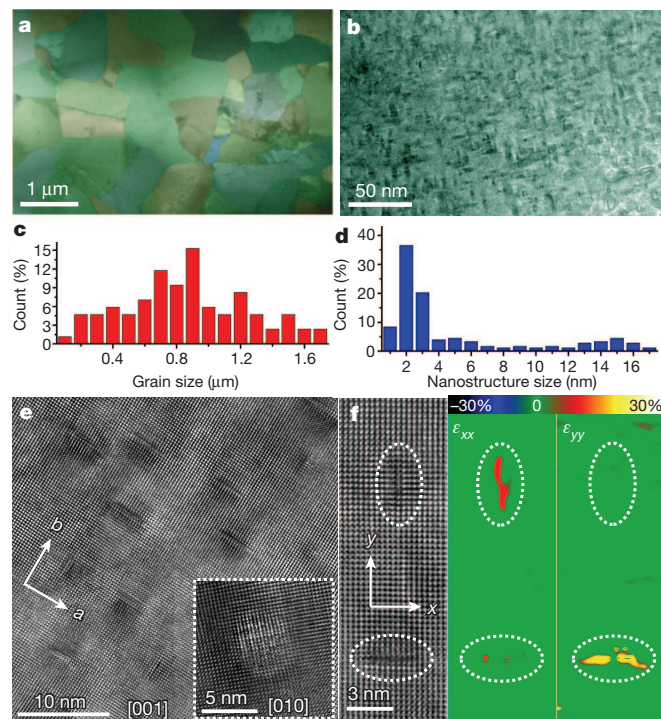


Figure 3 | Micro and nanostructures in SPS PbTe–SrTe(4 mol%) doped with 2 mol% Na. **a**, Low-magnification TEM image showing mesoscale grains in the sample. **b**, Medium-magnification TEM image revealing presence of platelet-like and spherical/ellipsoidal nanoscale precipitates. **c**, Grain size distribution histogram. **d**, Size distribution histogram of SrTe nanoparticles. **e**, High-magnification lattice image depicting some perpendicular or parallel platelet-like precipitates. Inset, a small spherical precipitate with a coherent interface with the matrix. **f**, Lattice image and strain maps showing elastic strain (colour scale) along only one direction for platelet-like precipitates. The estimate of the distribution density of all types of nanoscale precipitates is $\sim 1.2 \times 10^{12} \text{ cm}^{-2}$.

respectively). Figures 3c and 3d show the size distribution histogram of the mesoscale grains and nanoscale precipitates, respectively: the average size of the mesoscale grains is $\sim 0.8 \mu\text{m}$ and that of the nanoscale precipitates is $\sim 2.8 \text{ nm}$.

Figure 3e shows a representative high-resolution TEM image of platelet-like precipitates obtained with the electron beam parallel to the [001] axis. All platelet-like precipitates are organized perpendicular or parallel to each other, consistent with two of three possible crystallographic variants. The inset image, taken from a different region, shows a small spherical precipitate with a coherent (elastically strained) interface with the matrix, without any interfacial dislocations. To analyse the possible strain at and near the precipitate–matrix interface, the high-quality, high-resolution TEM images were analysed by geometric phase analysis²⁶, which is a semi-quantitative lattice image-processing approach for revealing spatially distributed strain fields. Figure 3f shows the image and the results of the analysis, namely the components ε_{xx} and ε_{yy} of the strain. The image shows two perpendicular platelet-like precipitates enclosed by dotted lines, and indicates that there is elastic strain only along the x direction for the upper precipitate and only along the y direction for the lower. Thus, the strain distribution in platelet-like precipitates is anisotropic, in contrast to spherical precipitates, which have more-uniform omnidirectional strain distributions.

Scanning TEM investigations (Fig. 4a) show the presence of some medium-size (20–50-nm) precipitates, in addition to smaller ones (1–15 nm). Energy dispersion X-ray spectroscopy indicates a large increase in the Sr signal from the precipitates (Fig. 4a, black curve in inset) compared to the matrix regions (Fig. 4a, blue curve in inset), suggesting that they are mainly SrTe.

The presence of SrTe nanoscale precipitates in the PbTe matrix was confirmed independently by APT²⁷. The three-dimensional reconstruction of the volume of the sample of PbTe–SrTe(4 mol%) doped

with 2% Na analysed by APT is given in Fig. 4b. The compositions of the matrix and the precipitates correspond to SrTe and PbTe, respectively (Supplementary Table 3). The composition profile across the interface of the large precipitate is measured using a proximity histogram (Fig. 4c), which shows $\sim 1.6 \text{ at}\%$ Na accumulation at the interface. There is also a slight Na concentration gradient in the matrix, with a lower concentration near the interface than in the bulk of the matrix. Sodium also accumulates at the core of a linear defect in the same reconstructed volume; that is, there is segregation at the dislocation core. Sodium was also observed to segregate at grain boundaries (Fig. 4d and Supplementary Fig. 8). We believe that the Na which is confined to grain boundaries (and other defect sites) at low temperature goes back into solid solution with the PbTe matrix at elevated temperatures, thus increasing the p-type charge-carrier density. This provides a viable explanation for the enhanced electrical conductivity (and power factor) of SPS samples at high temperature as discussed above (Fig. 2). Fitting the experimental diffusion coefficient, D , to $1/T$ data for Na in PbTe (ref. 28) and extrapolating to lower temperatures yields $D = 1.0 \times 10^{-16} \text{ cm}^2 \text{ s}^{-1}$ and $D = 3.6 \times 10^{-14} \text{ cm}^2 \text{ s}^{-1}$ at 550 and 650 K, respectively. Thus, the root mean square diffusion distance ($\sqrt{4Dt}$, where t is the diffusion time) of Na is $\sim 10 \text{ nm}$ for $t = 40 \text{ min}$ at 550 K and for $t = 7 \text{ s}$ at 650 K. This can be considered the temperature range for the onset of Na diffusion in Na-doped PbTe, which results in the observed plateaux, starting at $\sim 650 \text{ K}$, in σ and S as functions of T (Fig. 2a, b, arrows).

The panoscopic approach goes beyond nanostructuring and takes advantage of all relevant length scales by including the effects of mesoscale grain boundaries, endotaxial nanostructuring and atomic-scale substitutional doping in a bulk material. In this way, more extensive phonon scattering can be achieved and thermoelectric performance can be maximized. The p-type PbTe–SrTe system illustrates the important role (at high temperature) of grain-boundary phonon

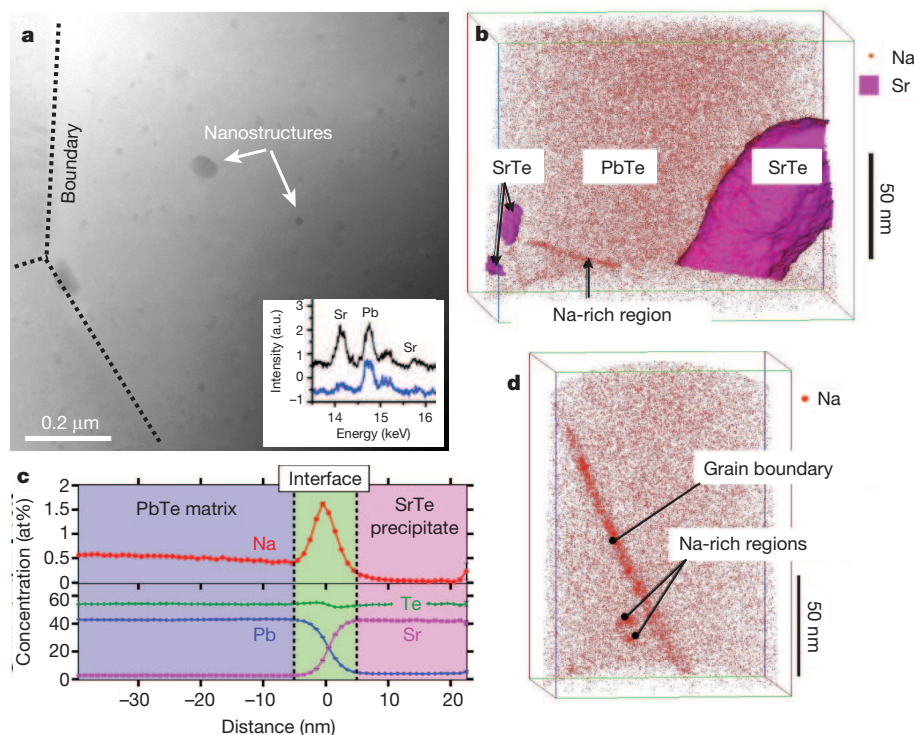


Figure 4 | Compositional analysis of SPS PbTe–SrTe(4 mol%) doped with 2 mol% Na. **a**, Scanning TEM image showing the presence of SrTe nanostructures in the PbTe matrix. Inset, energy dispersive X-ray spectrum (black, precipitate; blue, matrix). a.u., arbitrary units. **b**, Three-dimensional reconstruction of the volume analysed by APT (for clarity, only half of the Na atoms are displayed). SrTe precipitates are highlighted using a 25 at% Sr

isoconcentration surface. **c**, Proximity histogram showing the concentration profiles of Pb, Te, Sr and Na across the interface of the large SrTe precipitate. **d**, Three-dimensional reconstruction of a volume, analysed by APT, containing a grain boundary (for clarity, only the Na atoms are displayed). The volume is viewed from a direction parallel to the grain boundary.

scattering, which, in combination with nanostructuring, decreases κ_{lat} to levels well below those that can be reached by endotaxial nanostructuring alone. This is coupled to the added benefit of carrier generation at elevated temperatures through the dissolution of otherwise grain-boundary-confined Na into the bulk matrix at lower temperatures. Thus, a ZT value of ~ 2.2 at 915 K is readily and consistently achievable. The hierarchical architecture approach described here is expected to be applicable to any bulk thermoelectric system. With this advance in the maximum figure of merit, we can expect average ZT values of ~ 1.2 and ~ 1.7 for non-segmented and segmented thermoelectric devices, respectively ($ZT \approx 1.2$ at 350 K for segmentation with BiSbTe (ref. 6)). Considering a thermoelectric device with a cold-side temperature of 350 K and a hot-side temperature of 950 K, respective waste-heat conversion efficiencies^{3,4} of $\sim 16.5\%$ and $\sim 20\%$ are predicted. This may open realistic pathways to broad-based applications in automotive, military and marine waste-heat recovery.

METHODS SUMMARY

Several samples of PbTe–SrTe(0–4 mol%) doped with 2 mol% Na were synthesized first in the form of bulk ingots by melting at 1,323 K over 10 h, quenching to room temperature (297 K), followed by powder processing (Retsch RM200, Retsch GmbH) and spark plasma sintering (SPS 10-4, Thermal Technology LLC) at 823 K for 10 min under an axial pressure of 60 MPa in an argon atmosphere (supplementary, experimental). The σ and S were measured simultaneously in a helium atmosphere at temperatures ranging from room temperature to about 923 K on a ULVAC-RIKO ZEM-3 instrument system. We determined carrier concentrations using measurements of Hall coefficients at room temperature with a home-built system in applied magnetic fields ranging from 0 to 1.25 T. The thermal diffusivity, D , was directly measured in the temperature range 300–923 K by using the laser flash diffusivity method in a commercial Netzsch LFA-457 instrument. The thermal diffusivity was measured along the same direction as was the electrical transport. The heat capacity, C_p , was determined on the basis of previous reported experimental literature for PbTe (refs 11, 29). The total thermal conductivity was calculated using the formula $\kappa_{\text{total}} = DC_p\rho$, where ρ is the sample density, measured by gas pycnometer (Micromeritics AccuPyc 1340).

Received 31 March; accepted 24 July 2012.

- Snyder, J. G. & Toberer, E. S. Complex thermoelectric materials. *Nature Mater.* **7**, 105–114 (2008).
- Chen, G., Dresselhaus, M. S., Dresselhaus, G., Fleurial, J. P. & Caillat, T. Recent development in thermoelectric materials. *Int. Mater. Rev.* **48**, 45–66 (2003).
- Sootsman, J., Chung, D. Y. & Kanatzidis, M. G. New and old concepts in thermoelectric materials. *Angew. Chem. Int. Ed.* **48**, 8616–8639 (2009).
- Rowe, D. M. *CRC Handbook of Thermoelectrics: Macro to Nano* (CRC/Taylor & Francis, 2006).
- Tritt, T. M. (ed.) *Recent Trends in Thermoelectric Materials Research I* (Semiconductors and Semimetals Vol. 69, Academic, 2000); *Recent Trends in Thermoelectric Materials Research II* (Semiconductors and Semimetals Vol. 70, Academic, 2000); *Recent Trends in Thermoelectric Materials Research III* (Semiconductors and Semimetals Vol. 71, Academic, 2001).
- Poudel, B. *et al.* High-thermoelectric performance of nanostructured bismuth antimony telluride bulk alloys. *Science* **320**, 634–638 (2008).
- Venkatasubramanian, R., Siivola, E., Colpitts, V. & O'Quinn, B. Thin-film thermoelectric devices with high room-temperature figures of merit. *Nature* **413**, 597–602 (2001).
- Hsu, K. F. *et al.* Cubic AgPb_mSbTe_{2+m}: bulk thermoelectric materials with high figure of merit. *Science* **303**, 818–821 (2004).
- Poudeu, P. F. P. *et al.* High thermoelectric figure of merit and nanostructuring in bulk p-type Na_{1-x}Pb_mSb_yTe_{2+m}. *Angew. Chem. Int. Ed.* **45**, 3835–3839 (2006).
- Girard, S. N. *et al.* High performance Na-doped PbTe–PbS thermoelectric materials: electronic density of states modification and shape-controlled nanostructures. *J. Am. Chem. Soc.* **133**, 16588–16597 (2011).
- Pei, Y. *et al.* Convergence of electronic bands for high-performance bulk thermoelectric. *Nature* **473**, 66–69 (2011).
- Heremans, J. P. *et al.* Enhancement of thermoelectric efficiency in PbTe by distortion of the electronic density of states. *Science* **321**, 554–557 (2008).
- Shi, X. *et al.* Multiple-filled skutterudites: high thermoelectric figure of merit through separately optimizing electrical and thermal transport. *J. Am. Chem. Soc.* **133**, 7837–7846 (2011).
- Biswas, K. *et al.* Strained endotaxial nanostructures with high thermoelectric figure of merit. *Nature Chem.* **3**, 160–166 (2011).
- Zhu, G. H. *et al.* Increased phonon scattering by nanograins and point defects in nanostructured silicon with a low concentration of germanium. *Phys. Rev. Lett.* **102**, 196803 (2009).
- Martin, J., Wang, L., Chen, L. & Nolas, G. S. Enhanced Seebeck coefficient through energy-barrier scattering in PbTe nanocomposite. *Phys. Rev. B* **79**, 115311 (2009).
- Ravich, Y. I., Efimova, B. A. & Smirnov, I. A. *Semiconducting Lead Chalcogenides* Vol. 5 184–192 (Plenum, 1970).
- Crocker, A. J. & Rogers, L. M. Valence band structure of PbTe. *J. Phys. Colloq.* **29** (C4) 129–132 (1968).
- Airapetyants, S. V. & Vinogradova, M. N. Durbrovskaya, I. N., Kolomoets, N. V. & Rudnik, I. M. Structure of the valence band of heavily doped lead telluride. *Sov. Phys. Solid State* **8**, 1069–1072 (1966).
- Johnsen, S. *et al.* Nanostructures boost the thermoelectric performance of PbS. *J. Am. Chem. Soc.* **133**, 3460–3470 (2011).
- May, A. F., Fleurial, J.-P. & Snyder, G. J. Thermoelectric performance of lanthanum telluride produced via mechanical alloying. *Phys. Rev. B* **78**, 125205 (2008).
- Goldsmid, H. J. *Thermoelectric Refrigeration* (Plenum, 1964).
- Qiu, B., Bao, H., Zhang, G., Wu, Y. & Ruan, X. Molecular dynamics simulations of lattice thermal conductivity and spectral phonon mean free path of PbTe: bulk and nanostructures. *Comput. Mater. Sci.* **53**, 278–285 (2012).
- Tian, Z. *et al.* Phonon conduction in PbSe, PbTe and PbTe_{1-x}Se_x from first-principle calculations. *Phys. Rev. B* **85**, 184303 (2012).
- Esfarjani, K., Chen, G. & Stokes, H. T. Heat transport in silicon from first-principle calculations. *Phys. Rev. B* **84**, 085204 (2011).
- Hýtch, M. J., Snoeck, E. & Kilaas, R. Quantitative measurement of displacement and strain fields from HREM micrographs. *Ultramicroscopy* **74**, 131–146 (1998).
- Seidman, D. N. Three-dimensional atom-probe tomography: advances and applications. *Annu. Rev. Mater. Res.* **37**, 127–158 (2007).
- Crocker, A. J. & Dorning, B. F. Diffusion of sodium in lead telluride. *J. Phys. Chem. Solids* **29**, 155–161 (1968).
- Blachnik, R. & Igel, R. Thermodynamic properties of IV–VI compound: lead chalcogenides. *Z. Naturforsch. B* **29**, 625–629 (1974).

Supplementary Information is available in the online version of the paper.

Acknowledgements This work was supported by the Energy Frontier Research Center for Revolutionary Materials for Solid State Energy Conversion, funded by the US Department of Energy, Office of Science, Basic Energy Sciences under award number DE-SC0001054. TEM was performed in the (EPIC) (NIFTI) (Keck-II) facility of the NUANCE Center at Northwestern University. The spark plasma sintering system at Michigan State University is supported by ONR DURIP. APT was performed at NUCAPT and supported by NSF-MRI (DMR-0420532), ONR-DURIP (N00014-0400798, N00014-0610539, N00014-0910781), MRSEC (DMR-1121262) and ISEN at Northwestern University.

Author Contributions K.B. synthesized the samples and designed and carried out thermoelectric experiments. J.H. performed the TEM experiments. I.D.B. performed the APT measurements. C.-I.W. and T.P.H. performed the spark plasma sintering. K.B., J.H., I.D.B., D.N.S., V.P.D. and M.G.K. conceived the experiments, analysed the results and wrote and edited the manuscript.

Author Information Reprints and permissions information is available at www.nature.com/reprints. The authors declare no competing financial interests. Readers are welcome to comment on the online version of the paper. Correspondence and requests for materials should be addressed to M.G.K. (m-kanatzidis@northwestern.edu).

CORRIGENDUM

doi:10.1038/nature11645

Corrigendum: High-performance bulk thermoelectrics with all-scale hierarchical architectures

Kanishka Biswas, Jiaqing He, Ivan D. Blum, Chun-IWu, Timothy P. Hogan, David N. Seidman, Vinayak P. Dravid & Mercouri G. Kanatzidis

Nature **489**, 414–418 (2012); doi:10.1038/nature11439

In this Letter, the units of thermal conductivity on the *y*-axes of Fig. 2d and e should be $\text{W m}^{-1} \text{K}^{-1}$ and the *y*-axis label of Fig. 3d should be 'Count (%)'. Figures 2 and 3 of the original paper have been corrected online.